Mol. Cryst. Liq. Cryst., Vol. 527: pp. 98/[254]–108/[264], 2010

ISSN: 1542-1406 print/1563-5287 online
DOI: 10.1080/15421406.2010.486705

Taylor & Francis
Taylor & Francis Group

Nematicons in Liquid Crystal Light Valves

GAETANO ASSANTO,[1] ARMANDO PICCARDI,[1] ALESSANDRO ALBERUCCI,[1] STEFANIA RESIDORI,[2] AND UMBERTO BORTOLOZZO[2]

[1]NooEL, Nonlinear Optics and Opto-Electronics Laboratory, University "Roma Tre", Via della Vasca Navale, Rome, Italy
[2]INLN, Université de Nice Sophia-Antipolis, CNRS, Route des Lucioles, Valbonne, France

We demonstrate that photoconductive light valves with nematic liquid crystals support the propagation of spatial solitons and provide a convenient and effective environment for their all-optical routing and switching by means of external illumination.

Keywords Liquid crystals; nonlinear optics; reorientational response; signal routing; spatial solitons

Introduction

Spatial optical solitons are a rather innovative all-optical route for signal transfer and processing, as these self-confined beams can also trap weaker signals of different wavelengths. Controlling the trajectory of spatial solitons can therefore be considered a revolutionary approach to information routing, switching, processing [1–4]. In the past decade, nematic liquid crystals (NLC) have been clearly shown to provide an excellent platform for the investigation of optical soliton physics in both fundamental and applied aspects, including several avenues to soliton and soliton-waveguide routing, switching and gating [5–17]. A large fraction of the experiments carried out with solitons in NLC has been carried out in planar glass cells with thin film transparent electrodes for the application of a bias and the tuning of linear and nonlinear NLC properties [18]. All-optical soliton perturbations have also been implemented with external beams impinging orthogonally to the confining plates, i.e., nonlinearly inducing lens-like defects on or nearby the soliton path in the thickness of the cell [19–21]. An alternative configuration for soliton generation, propagation and deviations in NLC has been recently introduced by the use of liquid crystal light valves (LCLV) with a photoconductive layer [22], the latter meant to transform an external illumination into an adjustable voltage bias across the NLC [23–25]. However, spot-like illumination and beams can also be employed,

Address correspondence to Gaetano Assanto, NooEL, Nolinear Optics and Opto-Electronics Laboratory, University "Roma Tre", Via della Vasca Navale 84, Rome 00146, Italy. E-mail: assanto@uniroma3.it

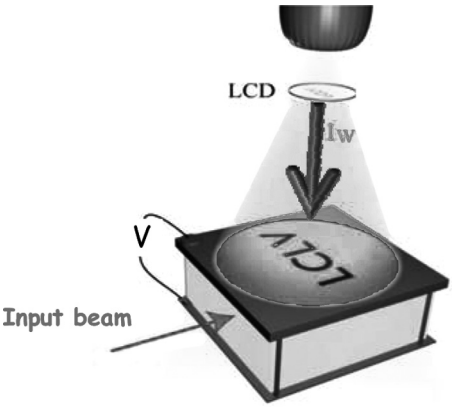

Figure 1. Sketch of a voltage biased photoconductive LCLV with external illumination and a beam launched in the NLC thickness in order to excite a nematicon. The shape of the external illumination can be programmed via the LCD.

impinging on the valve and locally altering the resistance of the photoconductive layer – i.e., the voltage bias- just under the shone region. Figure 1 is a pictorial representation of an illuminated LCLV with a soliton launched in its NLC thickness.

In this article we describe spatial soliton deviation by means of lens-like perturbations externally induced in the light valve by light-spots produced by a spatial light modulator (a liquid crystal display, LCD). In the next section we derive a suitable model to describe the interaction of self-confined optical waves in NLC ("nematicons" [26]) with these graded index lenses in the bulk medium. In the last section we will illustrate the experiments and a couple of potential applications of nematicons to signal routing and logic gates.

Model and Calculation of the Director Profile

Let us consider the LCLV sketched in Figure 1 and further detailed in Figure 2. A layer of NLC E48 is sandwiched between two slides parallel to the plane yz and spaced by L. The slides are rubbed in order to anchor the NLC molecular director at an angle $\varphi_0 = \pi/4$ with respect to z on the plane yz. A small pre-tilt in xz ($<2^\circ$) is introduced to avoid disclinations and eliminate the Freedericks threshold. Indium-Tin-Oxide (ITO) planar electrodes are deposited on the slides to allow applying a bias V_{bias} at low-frequency (<1 kHz). A layer of a photoconductor (we used Bismuth-Silicon-Oxide, BSO) defines one of the internal interfaces, i.e., a glass slide the other. Light at $\lambda = 514$ nm, hereafter called control beam, impinges from the top on the LCLV (Figs. 2(c-d)), inducing photo-generated charges in BSO; such charges reduce the BSO resistivity proportionally to the control intensity, therefore increasing the effective voltage drop acting on the underlying NLC [27]. In order to determine the molecular director distribution, we have to compute the two angles θ and φ (see Fig. 2) throughout the bulk NLC when a soliton propagates in the valve. For this extent, we set $\theta = \theta_{Vc} + \theta_b$ and $\varphi = \varphi_{Vc} + \varphi_b$, with $\theta_{Vc} = \theta_V + \theta_c$ and $\varphi_{Vc} = \varphi_V + \varphi_c$ the background values due to V_{bias} (θ_V, φ_V) and to the control beam (θ_c, φ_c), respectively; θ_b and φ_b are the nonlinear (reorientational) perturbations induced by the

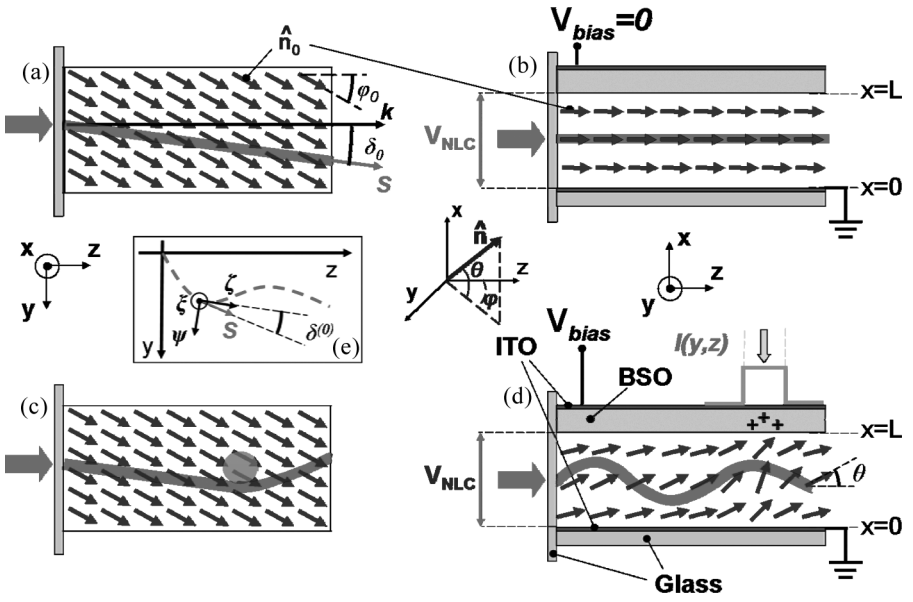

Figure 2. Sketch of the LCLV. (a) and (b) show the soliton evolution in the planes *yz* and *xz*, respectively, when no voltage is applied to the LCLV. (c) and (d) show the soliton deflection in the planes *yz* and *xz*, respectively, due to an impinging control beam and a non-null V_{bias}. (e) Reference system $\xi\psi\zeta$ which moves with the soliton trajectory (dashed line); to help the visualization, the beam is supposed to evolve in the plane *yz*. ***S*** is the Poynting vector, tangent on each point of the soliton path.

spatial soliton. The soliton-induced perturbations for typical experimental powers (<3mW) are negligible with respect to θ_{Vc}, hence $\theta \cong \theta_{Vc}$. Assuming an infinitely extended cell in the plane *yz*, it is $\theta_V = \theta_V(x)$ and $\varphi_V = \varphi_0$ throughout the NLC volume.

The low-frequency electric field $\boldsymbol{E}_{LF}$ effectively acting on the NLC is increased by the control-beam induced charges, due to the associated decrease in BSO resistivity. To first approximation we can set $V_{NLC}(y, z) = \Gamma V_{bias} + \alpha I(y, z)$, being V_{NLC} the drop voltage on the NLC (Fig. 2), Γ the bias partition between NLC and BSO layers, α an empirical constant. In the previous expression we did not account for variations of the intensity I along x, given that diffraction in the BSO can be neglected. We also assume that the low-frequency electric field components lying in the plane *yz* are negligible with respect to the *x*-component, i.e., $\boldsymbol{E}_{LF} = E_{LF}\hat{x}$. This is physically sensible because, owing to the geometry and the larger dielectric constant of BSO with respect to NLC ($\varepsilon_{BSO} = 56, \varepsilon_{\|} = 19.5$), [27] the field lines in *yz* concentrate in the BSO; hence, only θ_{Vc} changes under the action of $\boldsymbol{E}_{LF}$. Making the single elastic constant approximation, [28] the reorientation equation in 3D takes the form

$$\nabla^2 \theta_{Vc} + \gamma \sin(2\theta_{Vc}) E_{LF}^2 = 0 \tag{1}$$

with $\gamma = \varepsilon_0 \varepsilon_a / (2K)$, ε_0 the vacuum permittivity, ε_a the low-frequency NLC anisotropy and K the Frank elastic constant. In Eq. (1) the torques due to direct coupling between the control beam and induced dipoles in the NLC molecules can be

neglected for typical intensities (see the next section). Equation (1) must be solved with the proper boundary conditions. In $x=0$ and $x=L$ we have $\theta_{Vc}=\theta_0$, with θ_0 the pre-tilt angle imposed by rubbing at the surfaces parallel to yz. For directions in the plane yz we have $\lim_{|r_\perp|\to\infty}\theta_{Vc}(x,y,z)=\theta_V(x,\Gamma V_{bias})$, with $r_\perp=\sqrt{y^2+z^2}$. Due to the problem symmetry, we can expand the reorientation angle in a Fourier series along x, i.e., $\theta_{Vc}=\theta_0+\sum_n \theta_n(y,z)\sin\left(\frac{\pi n}{L}x\right)$. For the coefficients θ_n we get

$$\nabla^2_{yz}\theta_n-\left(\frac{\pi n}{L}\right)^2\theta_n+\frac{2}{L}\gamma E^2_{LF}(y,z)\int_0^L \sin\left[2\sum_m \theta_m \times \sin\left(\frac{\pi m}{L}x\right)\right]\sin\left(\frac{\pi n}{L}x\right)dx=0,\ (n=1,2,3...) \tag{2}$$

with $\nabla^2_{yz}=\partial^2/\partial z^2+\partial^2/\partial y^2$ and where we set $E_{LF}(y,\,z)=V_{NLC}/L$, i.e., a constant electric field along x. Equations (2) are a set of coupled nonlinear partial differential equations in 2D equivalent to our 3D problem. Noteworthy, the coupling between different θ_n stems from the nonlinearity due to the sine term in Eq. (1). The boundary conditions for θ_n can be easily found by expanding θ_V in a Fourier series. Equations (2) can be numerically integrated by using a standard Gauss-Seidel procedure enhanced by successive over-relaxation; the number of 2D equations to be solved to get a good accuracy is obtained by direct comparison with the complete profile (given by the sum on all previous coefficients). For the control beam we consider a circular flat-top profile, as in the experiments (see experimental section); thus, assuming a control beam centered in $(y,\,z)=(0,0)$, we set $\alpha I=\Delta V\mathrm{circ}(r_\perp/R)$, with the function circ equal to 1 for $r_\perp\le R$ and zero elsewhere. An example of the obtained profiles of reorientation angle is displayed in Figure 3.

The maximum soliton deflection is achieved when ΔV is high enough to saturate the angle distribution; in this case the index perturbation is maximized.

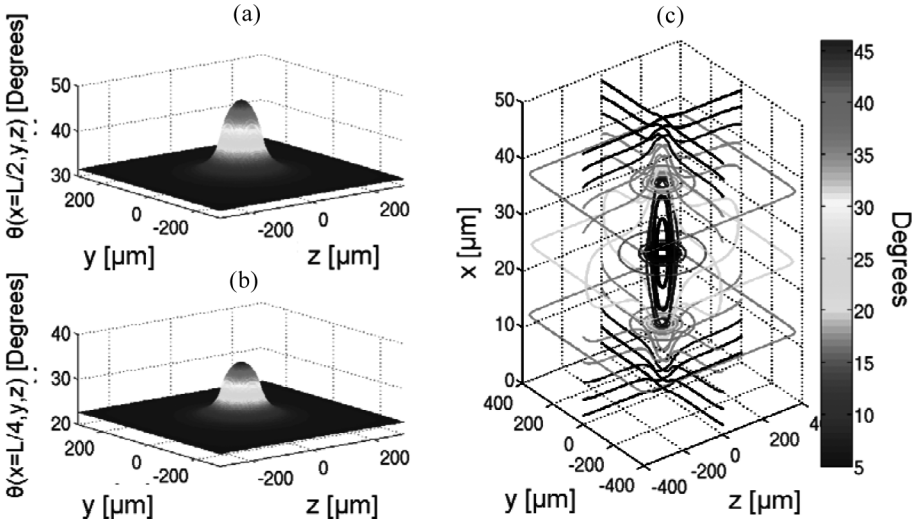

Figure 3. Numerically computed three-dimensional θ_{Vc} profile. (a) and (b) graph the θ_{Vc} distribution in the planes $x=L/2$ and $x=L/4$, respectively; (c) shows the 3D contour plot for θ_{Vc}. In this simulation we set $\Gamma V_{bias}=1\,\mathrm{V}$, $\Delta V=0.2\,\mathrm{V}$, $R=50\,\mu\mathrm{m}$ and $L=50\,\mu\mathrm{m}$.

The profile θ_{Vc} can be conveniently derived as a collection of one-dimensional solutions, i.e., θ_V, using in each point (y, z) an equivalent voltage drop $V_{NLC}^{eq}(y, z)$ on the NLC obtained by a comparison with the exact solution from Eq. (2). Owing to the high nonlocality of the medium, [28] $V_{NLC}^{eq}(y,z)$ will be wider than the control beam; hence, we can write $\theta_{Vc}(x,y,z) = \theta_V(x, V_{NLC}^{eq}(y,z))$ and consider $\alpha I = \Delta V \mathrm{sech}[(r_\perp - R_{fit})/w]$ for $r_\perp \geq R_{fit}$ and $\alpha I = \Delta V$ for $r_\perp < R_{fit}$, with R_{fit} and w fit parameters for width and boundary slope, respectively. The accuracy of this approximation can be appreciated in Figure 4, showing the comparison between full numerical simulation and semi-analytical approximation.

The reorientational nonlinearity acts and depends on the extraordinary-wave component (for power below the Freedericksz threshold [5, 10–12]); thus, reorientational spatial solitons in liquid crystals are extraordinarily-polarized beams. Furthermore, in the geometry sketched in Figure 2 the range of nonlocality is fixed by the smallest cell dimension, given by L; we take $L = 50\,\mu\mathrm{m}$ (see Figs. 3 and 4), implying that variations in the director profile occur on a length scale given by L, independently from the size of the external excitation. Hence, director variations are slow enough to ensure no coupling between ordinary and extraordinary (soliton) components (i.e., the Mauguin limit applies [28]), as verified in the experiments.

To describe the soliton propagation, we define a moving reference $\xi\psi\zeta$ with ζ parallel to the local soliton wavevector, ξ the direction of the ordinary polarization and $\hat{\zeta} = \hat{\xi} \times \hat{\psi}$ (Fig. 2(e)). Within the NLC region interested by the soliton and due to the adiabatic θ, the electric permittivity $\boldsymbol{\varepsilon}$ can be cast as $\boldsymbol{\varepsilon} = [\varepsilon_{\xi\xi}, 0, 0; 0, \varepsilon_{\psi\psi}, \varepsilon_{\psi\zeta}; 0, \varepsilon_{\zeta\psi}, \varepsilon_{\zeta\zeta}]$. We write the e-field as $\boldsymbol{E}_e = E e^{ik_0 n_e^{(0)} \zeta} \hat{t}$, with k_0 the vacuum wavenumber, $n_e^{(0)}$ and $\hat{t}$ refractive index and polarization versor of the corresponding

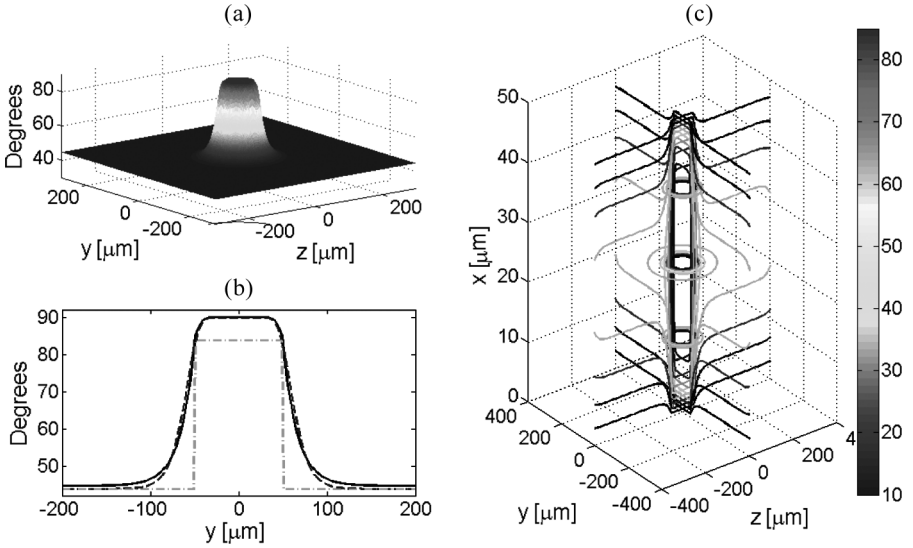

Figure 4. (a) θ_{Vc} distribution in the plane $x = L/2$. (b) θ_{Vc} versus y from the complete 3D simulation (solid line) and its semi-analytical approximation $\theta_V(x, V_{NLC}^{eq}(y,z))$ (dashed line). The dashed-dotted line is the control-beam profile. (c) 3D contour plot of the numerical solution. In this case we took $R = 50\,\mu\mathrm{m}$, $\Delta V = 3\,\mathrm{V}$ and $\Gamma V_{\mathrm{bias}} = 1.1\,\mathrm{V}$. The fit-parameters are $R_{fit} = 30\,\mu\mathrm{m}$ and $w = 11\,\mu\mathrm{m}$.

e-polarized plane-wave (at the peak of the beam spectrum), respectively. If $\delta^{(0)}$ is the walk-off, a new reference ξts is obtained by rotating $\xi\psi\zeta$ by $\delta^{(0)}$ around ξ. In the paraxial approximation,

$$2in_e^{(0)}k_0\left[\frac{\partial E}{\partial\zeta}+\frac{D_{\psi\zeta}}{2D_\zeta}\frac{\partial E}{\partial\psi}\right]+\frac{1}{D_\zeta}\frac{\partial^2 E}{\partial\xi^2}+\frac{D_\psi}{D_\zeta}\frac{\partial^2 E}{\partial\psi^2}+k_0^2\Delta n_e^2 E=0 \tag{3}$$

The quantities $D_\zeta=-D_{1t}^{\zeta\zeta}+MD_{2t}^{\psi\psi}$, $D_\psi=-D_{1t}^{\psi\psi}+MD_{2t}^{\zeta\zeta}$, $D_{\psi\zeta}=-D_{1t}^{\psi\zeta}+MD_{2t}^{\psi\zeta}$ include the transverse distribution of the optic axis, with $M=\lfloor\varepsilon_{ts}-D_{1s}^{\zeta\zeta}(n_e^{(0)})^2\rfloor/\lfloor\varepsilon_{ss}-D_{2s}^{\zeta\zeta}(n_e^{(0)})^2\rfloor$ and

$$\begin{aligned}
D_{1t}^{\psi\psi}&=-\left(\frac{\varepsilon_{tt}}{\varepsilon_{\xi\xi\xi}}\cos^2\delta^{(0)}+\sin^2\delta^{(0)}+\frac{\varepsilon_{st}}{\varepsilon_{\xi\xi\xi}}\cos\delta^{(0)}\sin\delta^{(0)}\right)\\
D_{2t}^{\psi\psi}&=\left(1-\frac{\varepsilon_{tt}}{\varepsilon_{\xi\xi\xi}}\right)\cos\delta^{(0)}\sin\delta^{(0)}-\frac{\varepsilon_{st}}{\varepsilon_{\xi\xi\xi}}\sin^2\delta^{(0)}\\
D_{1t}^{\psi\zeta}&=-\left(1-\frac{\varepsilon_{tt}}{\varepsilon_{\xi\xi\xi}}\right)\sin\left(2\delta^{(0)}\right)-\frac{\varepsilon_{st}}{\varepsilon_{\xi\xi\xi}}\cos\left(2\delta^{(0)}\right)\\
D_{2t}^{\psi\zeta}&=\left(1-\frac{\varepsilon_{tt}}{\varepsilon_{\xi\xi\xi}}\right)\cos\left(2\delta^{(0)}\right)-\frac{\varepsilon_{st}}{\varepsilon_{\xi\xi\xi}}\sin\left(2\delta^{(0)}\right)\\
D_{1t}^{\zeta\zeta}&=-\left(\frac{\varepsilon_{tt}}{\varepsilon_{\xi\xi\xi}}\sin^2\delta^{(0)}+\cos^2\delta^{(0)}-\frac{\varepsilon_{st}}{\varepsilon_{\xi\xi\xi}}\cos\delta^{(0)}\sin\delta^{(0)}\right)\\
D_{2t}^{\zeta\zeta}&=\left(\frac{\varepsilon_{tt}}{\varepsilon_{\xi\xi\xi}}-1\right)\sin\delta^{(0)}\cos\delta^{(0)}-\frac{\varepsilon_{st}}{\varepsilon_{\xi\xi\xi}}\cos^2\delta^{(0)}\\
D_{1s}^{\zeta\zeta}&=\frac{\varepsilon_{st}}{\varepsilon_{\xi\xi\xi}}\sin^2\delta^{(0)}-\left(\frac{\varepsilon_{ss}}{\varepsilon_{\xi\xi\xi}}-1\right)\cos\delta^{(0)}\sin\delta^{(0)}\\
D_{2s}^{\zeta\zeta}&=\frac{\varepsilon_{ss}}{\varepsilon_{\xi\xi\xi}}\cos^2\delta^{(0)}+\sin^2\delta^{(0)}-\frac{\varepsilon_{st}}{\varepsilon_{\xi\xi\xi}}\cos\delta^{(0)}\sin\delta^{(0)}
\end{aligned}$$

n_e is the extraordinary refractive index for plane waves considering the local value of the director. The superscript "0" refers to the soliton center of mass $\bar{\boldsymbol{r}}_b=\int\int\boldsymbol{r}_b|E|^2d\xi d\psi/\int\int|E|^2d\xi d\psi$ ($\boldsymbol{r}_b=\xi\hat{\xi}+\psi\hat{\psi}$); hence, these quantities vary as the nematicon moves in the director landscape, but they do not depend on local transverse coordinates ψ and ξ. Δn_e^2 is the refractive index variation due to bias, control beams and solitons; if β is the (local) angle between the soliton wavevector and $\hat{\boldsymbol{n}}$, then $\Delta n_e^2=n_e^2(\beta)-n_e^2(\beta^{(0)})=n_e^2(\beta)-(n_e^{(0)})^2$ and accounts for both self-confinement (θ_b, φ_b) and index landscape (θ_{Vc}, φ_{Vc}).

Since $D_\psi^{(0)}/D_\zeta^{(0)}\approx 1/D_\zeta^{(0)}\approx 1$, Eq. (3) is equivalent to the Schrödinger equation for a charged particle in an electromagnetic field, with Hamiltonian $H=\frac{1}{2m}(\boldsymbol{p}-\frac{e}{c}\boldsymbol{A})^2+eU$ (m is the particle mass, e its charge, c the speed of light in vacuum, $\boldsymbol{p}$ the momentum, $\boldsymbol{A}$ and U the vector and scalar potentials, respectively). Thus, a transversally-varying force $\boldsymbol{F}$ acts on the soliton, with

$$\boldsymbol{F}=2k_0^2\left[\left(n_e\frac{\partial n_e}{\partial\xi}\right)\hat{\xi}+\left(n_e\frac{\partial n_e}{\partial\psi}\right)\hat{\psi}+\left(\left(n_e^{(0)}\right)^2\frac{\partial\tan\delta^{(0)}}{\partial\zeta}\right)\hat{\psi}\right] \tag{4}$$

directed normally to the wavevector. The first two terms on the RHS of Eq. (4) are due to index gradients as in isotropic media, the third is directed along ψ and characteristic of anisotropy: it accounts for longitudinal changes in walkoff. Finally, applying the Ehrenfest theorem, the soliton trajectory in the highly nonlocal limit is governed by

$$2k_0^2\left(n_e^{(0)}\right)^2 d^2\bar{\mathbf{r}}_b \Big/ d\zeta^2 = \boldsymbol{F}|_{\mathbf{r}_b=\bar{\mathbf{r}}_b} \tag{5}$$

Equation (5) predicts a soliton path independent on waist. From Eq. (5), the transverse force attracts the soliton towards the axis of the defect (induced by the control beam) because the *e*-refractive index is larger where V_{NLC} is higher, owing to the dominant director rotation in $x\hat{n}_0$. Figure 5 shows the soliton trajectory computed for a circular control beam shown in Figure 4. Figure 5(a) shows the soliton trajectory in the absence of external illumination: the soliton evolves with sinusoidal oscillations in xz due to the joint action of walk-off and of index-well created by ΓV_{bias} and bending the wavevector, with a resulting period of about 400 μm. In the plane yz the soliton appears to propagate straight, with slope $\tan(\delta_{yz})$, being δ_{yz} the apparent walk-off [11]. When a control beam impinges on BSO, the nematicon is deflected towards negative y according to Eq. (5), as visible in Figures 5(b–c). Figure 5(d) shows the refractive index "seen" by the propagating soliton, oscillating like the trajectory due to the varying molecular reorientation at each x and to wavevector bending. Finally, Figure 5(e) plots the change in wavevector along z: in

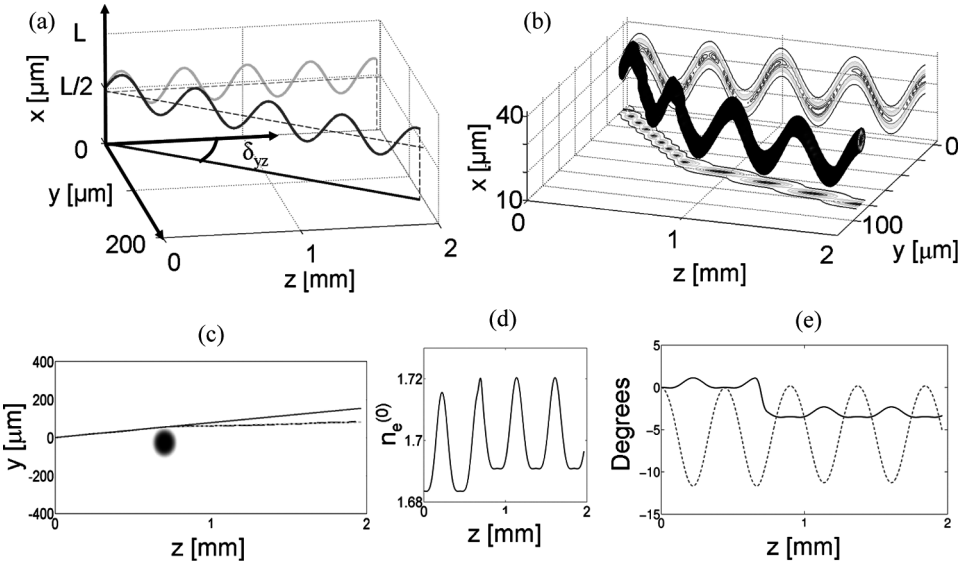

Figure 5. (a) Calculated 3D soliton trajectory without control beam and $\Gamma V_{bias} = 1.1$ V. δ_{yz} is the apparent walk-off. (b) Soliton path when a control beam in $y = -30$ μm, $z = 900$ μm and with $\Delta V = 3$ V and $R = 50$ μm. (c) Soliton trajectory in the plane yz with conditions as in (b): solid and dashed lines are the soliton paths with and without control beam, respectively; the black line is the experimental result with perturbation, the circle indicating the control spot. (d) Refractive index $n_e^{(0)}$ "seen" by the soliton versus z. (e) Wavevector azimuth φ_k (solid line) and elevation θ_k (dashed line) versus z (see angles defined for the director in Fig. 2).

the plane xz the wavevector is slightly affected by the introduced defect which, as expected, acts mainly in yz introducing a steering of nearly 5°. In the regions far removed from the defect (e.g., $z < 800\,\mu m$ and $z > 1.1\,mm$), the wavevector oscillates in yz due to the anisotropic nature of the medium, which couples index gradients along x with wavevector displacements on the plane yz.

Experiments

In an LCLV as described above, sketched in Figure 2, we coupled a He-Ne laser beam ($\lambda = 633\,nm$, wavelength at which BSO is insensitive) focusing it with a $20\times$ microscope objective in order to obtain an input waist of about $6\,\mu m$. Self-focusing at a power $P = 2mW$ ensured the formation of a nematicon, propagating in the plane yz with wavevector $\boldsymbol{k}//\boldsymbol{z}$ in the absence of external perturbations, either electrical or optical. Light from a solid state laser diode operating at $\lambda = 514\,nm$ was focused on the BSO layer to perturb the NLC. An LCD, operated as amplitude modulator, was employed to define size ($R = 50\,\mu m$), intensity ($100\,\mu W/cm^2$) and position of the control spot. A voltage $V_{bias} = 4.5\,V$ is applied to the sample, such value maximizing soliton deflection due to the BSO action [22]. Soliton evolution is observed collecting the out of plane scattered light with a microscope and a CCD camera. From the apparent walk-off in absence of control beam, we estimate $\Gamma V_{bias} = 1.1\,V$. In the described experimental conditions we obtained an excellent agreement between the experimental and computed trajectories on the plane yz (see Fig. 5(c)).

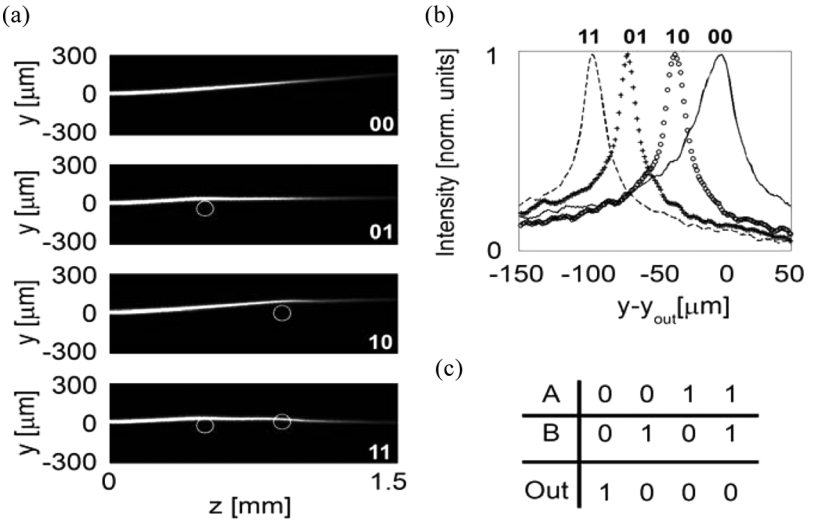

Figure 6. Soliton-based NOR logic gate. (a) Images of soliton evolution in yz for various states of control beams (bits) as indicated in white lettering. White circles indicate the control spots on the LCLV, located in $[y, z] = [-50, 500]\,\mu m$ and $[y, z] = [0, 900]\,\mu m$ for 01 and 10, respectively. (b) Output transverse intensity profiles of the soliton in $z = 1.5\,mm$, with the corresponding input states indicated above. Solid line, crosses, circles and dashes correspond to the image sequence in (a), from top to bottom. y_{out} is the output position of the unperturbed soliton, corresponding to the *high output*. (c) Truth table for the NOR gate.

The above shown large deflection of the soliton by means of a single defect, combined with the possibility to write an arbitrary set of defects, allows us implement strategies for all-optical digital signal processing, changing both their number and positions. For example, switching on (off) a control spot can be made to correspond to a *high/true* (*low/false*) digital input (bit), whereas the soliton outcome yields the *output* state. Using two control beams and associating the *high* logic value to an output position of the soliton along y, it is possible to realize standard logic gates.

As a first example we consider a NOR gate, with output *high* when both inputs are *low* (see Fig. 6(c)). It can be obtained by assigning the *high* output to the soliton y-position at rest (i.e., without perturbation(s)). This is visible in Figures 6(a–b): the presence of one (01, 10) or two (11) defects alter the nematicon trajectory and the *output* will not receive any soliton-carried signal, i.e., it will be recognized as a *low* bit (0). The transverse profiles experimentally acquired for the various input configuration of control-bits are shown in Figure 6(b): the separation between the peaks is well pronounced.

Another example is the XNOR, where the *output* should be *high* if the inputs are equal (00 or 11, see Figure 7(c)). In this case, as shown in Figures 7(a–b), the two control beams must be positioned in such a way as to compensate each other's effect when they are both *on*; the *high output* corresponding to the absence or perfect compensation of defects. If just one of the input bits is *high*, the soliton deviation makes the *output* 0, whereas the simultaneous presence of the two *high* inputs steers twice the soliton, back to the unperturbed output location and yielding a *high output*.

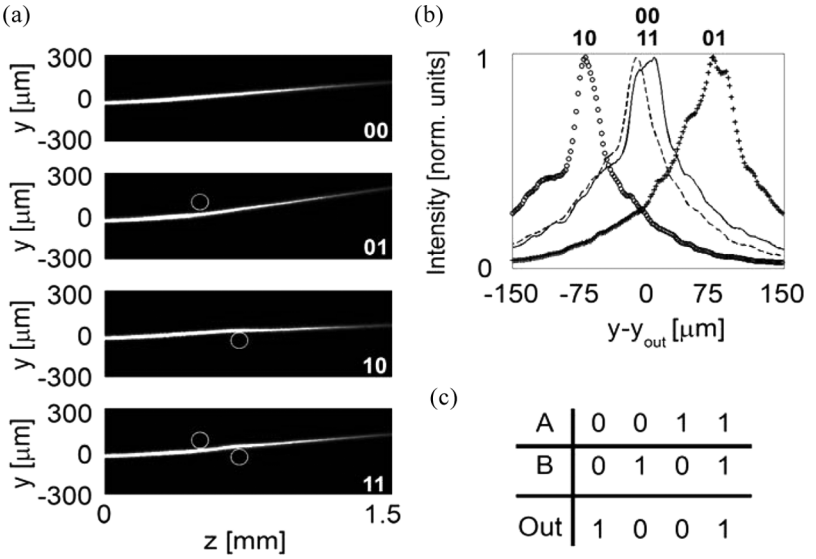

Figure 7. Soliton based XNOR logic gate. (a) Images of soliton evolution in yz without and with control spots centered in $[y, z] = [70, 500]\,\mu m$ and $[y, z] = [-20, 700]\,\mu m$ for 01 and 10, respectively. (b) Output transverse profiles of nematicon in $z = 1.5\,mm$, with corresponding input states indicated above. Solid line, crosses, circles and dashes correspond to the image sequence in (a), from top to bottom. y_{out} is the output position of the unperturbed soliton, corresponding to a *high output*. (c) Truth table for the XNOR gate.

Conclusions

We have shown that liquid crystal light valves with a photoconductive interface can be an ideal environment for excitation and trajectory-control of spatial optical solitons in nematic liquid crystals. Soliton steering can be conveniently obtained by illuminating the valve with external light spots, creating photo-carriers and -in turn- refractive defects able to perturb the soliton path in propagation. Such interaction between self-confined wavepackets and three-dimensional perturbation in index and optic axis distribution can be modeled using Maxwell equations and also adopting suitable approximations which account for the high nonlocality of the response. Semi-analytical approximation and complete numerical calculation are in very good agreement in the saturation limit which maximizes soliton deflection. Soliton trajectories can therefore be described accounting for anisotropy and dis-homogeneity by means of the Ehrenfest theorem, with an excellent agreement with the experimental results. Finally, the theoretical/numerical model allowed us to design soliton logic gates which could demonstrate experimentally in the light valve using green light for the control beams and red light for the nematicon. Using two control beams we reported on the realization of a NOR and an XNOR gates. Such findings will open avenues towards all-optical signal processing, gating, routing and switching using nematicons in LCLV.

Acknowledgments

We are grateful to the Italo-French University for supporting the collaboration between the two groups through a Galileo travel grant (2009).

References

[1] Snyder, A. W., Mitchell, D. J., & Ladouceur, F. (1991). *Opt. Lett.*, *10*, 21–23.
[2] Akhmediev, N. N. (1998). *Opt. Quantum Electron.*, *30*, 535–543.
[3] Stegeman, G. I., & Segev, M. (1999). *Science*, *286*, 1518.
[4] Conti, C., & Assanto, G. (2004). In: *Encyclopedia of Modern Optics*, Guenther, R. D., Steel, D. G., & Bayvel, L. (Eds.), Elsevier: Oxford, Vol. 5, 43–55.
[5] Peccianti, M., Assanto, G., De Luca, A., Umeton, C., & Khoo, I. C. (2000). *Appl. Phys. Lett.*, *77*, 7–9.
[6] Peccianti, M., & Assanto, G. (2001). *Opt. Lett.*, *26*, 1690–1692.
[7] Peccianti, M., & Assanto, G. (2002). *Phys. Rev. E (Rapid Commun.)*, *65*, 035603–035606.
[8] Peccianti, M., Brzdąkiewicz, K. A., & Assanto, G. (2002). *Opt. Lett.*, *27*, 1460–1462.
[9] Peccianti, M., Conti, C., Assanto, G., De Luca, A., & Umeton, C. (2002). *Appl. Phys. Lett.*, *81*, 3335–3337.
[10] Peccianti, M., Fratalocchi, A., & Assanto, G. (2004). *Opt. Express*, *12*(26), 6524–6529.
[11] Peccianti, M., Conti, C., Assanto, G., De Luca, A., & Umeton, C. (2004). *Nature*, *432*, 733–737.
[12] Peccianti, M., Assanto, G., Dyadyusha, A., & Kaczmarek, M. (2006). *Nat. Phys.*, *2*, 737–742.
[13] Peccianti, M., Assanto, G., Dyadyusha, A., & Kaczmarek, M. (2007). *Opt. Lett.*, *32*(3), 271–273.
[14] Peccianti, M., Assanto, G., Dyadyusha, A., & Kaczmarek, M. (2007). *Phys. Rev. Lett.*, *98*, 113902.
[15] Fratalocchi, A., Piccardi, A., Peccianti, M., & Assanto, G. (2007). *Opt. Lett.*, *32*(11), 1447–1449.

[16] Peccianti, M., & Assanto, G. (2007). *Opt. Express*, *15*(13), 8021–8028.
[17] Alberucci, A., Peccianti, M., & Assanto, G. (2007). *Opt. Lett.*, *32*(19), 2795–2797.
[18] Peccianti, M., Conti, C., & Assanto, G. (2005). *Opt. Lett.*, *30*(4), 415–417.
[19] Serak, S. V., Tabiryan, N. V., Peccianti, M., & Assanto, G. (2006). *IEEE Photon. Techn. Lett.*, *18*(12), 1287–1289.
[20] Pasquazi, A., Alberucci, A., Peccianti, M., & Assanto, G. (2005). *Appl. Phys. Lett.*, *87*, 261104.
[21] Piccardi, A., Assanto, G., Lucchetti, L., & Simoni, F. (2008). *Appl. Phys. Lett.*, *93*, 171104.
[22] Piccardi, A., Bortolozzo, U., Residori, S., & Assanto, G. (2009). *Opt. Lett.*, *34*, 737.
[23] Residori, S. (2005). Patterns, fronts and structures in a liquid-crystal-light-valve with optical feedback. *Phys. Rep.*, *416*, 201–272.
[24] Bortolozzo, U., Residori, S., & Huignard, J. P. (2008). *J. Phys. D: Appl. Phys.*, *41*, 224007.
[25] Bortolozzo, U., Residori, S., Petrosyan, A., & Huignard, J. P. (2006). *Opt. Commun.*, *263*, 317–321.
[26] Assanto, G., Peccianti, M., & Conti, C. (2003). *Opt. Photon. News*, *14*, 44–48.
[27] Gunter, P., & Huignard, J. P. (2006). *Photorefractive Materials and Their Applications 1*, Springer: New York.
[28] De Gennes, P. G., & Prost, J. (1993). *The Physics of Liquid Crystals*, Oxford Science: New York.
[29] Conti, C., Peccianti, M., & Assanto, G. (2004). *Phys. Rev. Lett.*, *92*, 113902.